

High speed spectral domain optical coherence tomography for retinal imaging at 500,000 A-lines per second

Lin An,¹ Peng Li,¹ Tueng T. Shen,^{2,1} and Ruikang Wang^{1,2,*}

¹Department of Bioengineering, University of Washington, Seattle, WA 98195, USA

²Department of Ophthalmology, University of Washington, Seattle, WA 98195, USA

*wangrk@uw.edu

Abstract: We present a new development of ultrahigh speed spectral domain optical coherence tomography (SDOCT) for human retinal imaging at 850 nm central wavelength by employing two high-speed line scan CMOS cameras, each running at 250 kHz. Through precisely controlling the recording and reading time periods of the two cameras, the SDOCT system realizes an imaging speed at 500,000 A-lines per second, while maintaining both high axial resolution ($\sim 8 \mu\text{m}$) and acceptable depth ranging ($\sim 2.5 \text{ mm}$). With this system, we propose two scanning protocols for human retinal imaging. The first is aimed to achieve isotropic dense sampling and fast scanning speed, enabling a 3D imaging within 0.72 sec for a region covering $4 \times 4 \text{ mm}^2$. In this case, the B-frame rate is 700 Hz and the isotropic dense sampling is 500 A-lines along both the fast and slow axes. This scanning protocol minimizes the motion artifacts, thus making it possible to perform two directional averaging so that the signal to noise ratio of the system is enhanced while the degradation of its resolution is minimized. The second protocol is designed to scan the retina in a large field of view, in which 1200 A-lines are captured along both the fast and slow axes, covering 10 mm^2 , to provide overall information about the retinal status. Because of relatively long imaging time (4 seconds for a 3D scan), the motion artifact is inevitable, making it difficult to interpret the 3D data set, particularly in a way of depth-resolved en-face fundus images. To mitigate this difficulty, we propose to use the relatively high reflecting retinal pigmented epithelium layer as the reference to flatten the original 3D data set along both the fast and slow axes. We show that the proposed system delivers superb performance for human retina imaging.

© 2011 Optical Society of America

OCIS codes: (170.4460) Ophthalmic optics and devices; (170.3880) medical and biological imaging; (170.4500) Optical coherence tomography

References and links

1. D. Huang, E. A. Swanson, C. P. Lin, J. S. Schuman, W. G. Stinson, W. Chang, M. R. Hee, T. Flotte, K. Gregory, C. A. Puliafito, and J. G. Fujimoto, "Optical coherence tomography," *Science* **254**(5035), 1178–1181 (1991).
2. A. F. Fercher, W. Drexler, C. K. Hitzenberger, and T. Lasser, "Optical coherence tomography - principles and applications," *Rep. Prog. Phys.* **66**(2), 239–303 (2003).
3. P. H. Tomlins and R. K. Wang, "Theory, developments and applications of optical coherence tomography," *J. Phys. D Appl. Phys.* **38**(15), 2519–2535 (2005).
4. A. F. Fercher, C. K. Hitzenberger, W. Drexler, G. Kamp, and H. Sattmann, "In vivo optical coherence tomography," *Am. J. Ophthalmol.* **116**(1), 113–114 (1993).
5. C. K. Hitzenberger, P. Trost, P. W. Lo, and Q. Y. Zhou, "Three-dimensional imaging of the human retina by high-speed optical coherence tomography," *Opt. Express* **11**(21), 2753–2761 (2003).
6. A. F. Fercher, C. K. Hitzenberger, G. Kamp, and S. Y. Elzaiat, "Measurement of intraocular distances by backscattering spectral interferometry," *Opt. Commun.* **117**(1-2), 43–48 (1995).
7. G. Häusler and M. W. Lindner, "Coherence radar' and 'spectral radar'-new tools for dermatological diagnosis," *J. Biomed. Opt.* **3**(1), 21–31 (1998).

8. S. R. Chinn, E. A. Swanson, and J. G. Fujimoto, "Optical coherence tomography using a frequency-tunable optical source," *Opt. Lett.* **22**(5), 340–342 (1997).
9. U. Haberland, P. Jansen, V. Blazek, and H. J. Schmitt, "Optical coherence tomography of scattering media using frequency-modulated continuous-wave techniques with tunable near-infrared laser," *Proc. SPIE* **2981**, 20–28 (1997).
10. J. F. de Boer, B. Cense, B. H. Park, M. C. Pierce, G. J. Tearney, and B. E. Bouma, "Improved signal-to-noise ratio in spectral-domain compared with time-domain optical coherence tomography," *Opt. Lett.* **28**(21), 2067–2069 (2003).
11. M. Choma, M. Sarunic, C. Yang, and J. Izatt, "Sensitivity advantage of swept source and Fourier domain optical coherence tomography," *Opt. Express* **11**(18), 2183–2189 (2003).
12. R. Leitgeb, C. Hitzenberger, and A. Fercher, "Performance of Fourier domain vs. time domain optical coherence tomography," *Opt. Express* **11**(8), 889–894 (2003).
13. M. Wojtkowski, R. Leitgeb, A. Kowalczyk, T. Bajraszewski, and A. F. Fercher, "In vivo human retinal imaging by Fourier domain optical coherence tomography," *J. Biomed. Opt.* **7**(3), 457–463 (2002).
14. B. Cense, N. Nassif, T. Chen, M. Pierce, S.-H. Yun, B. Park, B. Bouma, G. Tearney, and J. de Boer, "Ultra-high-resolution high-speed retinal imaging using spectral-domain optical coherence tomography," *Opt. Express* **12**(11), 2435–2447 (2004).
15. D. M. de Bruin, D. L. Burnes, J. Loewenstein, Y. Chen, S. Chang, T. C. Chen, D. D. Esmaili, and J. F. de Boer, "In vivo three-dimensional imaging of neovascular age-related macular degeneration using optical frequency domain imaging at 1050 nm," *Invest. Ophthalmol. Vis. Sci.* **49**(10), 4545–4552 (2008).
16. E. C. Lee, J. F. de Boer, M. Mujat, H. Lim, and S. H. Yun, "In vivo optical frequency domain imaging of human retina and choroid," *Opt. Express* **14**(10), 4403–4411 (2006).
17. H. Lim, M. Mujat, C. Kerbage, E. C. Lee, Y. Chen, T. C. Chen, and J. F. de Boer, "High-speed imaging of human retina in vivo with swept-source optical coherence tomography," *Opt. Express* **14**(26), 12902–12908 (2006).
18. M. Wojtkowski, V. Srinivasan, T. Ko, J. Fujimoto, A. Kowalczyk, and J. Duker, "Ultra-high-resolution, high-speed, Fourier domain optical coherence tomography and methods for dispersion compensation," *Opt. Express* **12**(11), 2404–2422 (2004).
19. R. Leitgeb, W. Drexler, A. Unterhuber, B. Hermann, T. Bajraszewski, T. Le, A. Stingl, and A. Fercher, "Ultra-high resolution Fourier domain optical coherence tomography," *Opt. Express* **12**(10), 2156–2165 (2004).
20. V. J. Srinivasan, R. Huber, I. Gorczynska, J. G. Fujimoto, J. Y. Jiang, P. Reisen, and A. E. Cable, "High-speed, high-resolution optical coherence tomography retinal imaging with a frequency-swept laser at 850 nm," *Opt. Lett.* **32**(4), 361–363 (2007).
21. A. H. Bachmann, M. L. Villiger, C. Blatter, T. Lasser, and R. A. Leitgeb, "Resonant Doppler flow imaging and optical vivisection of retinal blood vessels," *Opt. Express* **15**(2), 408–422 (2007).
22. L. An and R. K. Wang, "In vivo volumetric imaging of vascular perfusion within human retina and choroids with optical micro-angiography," *Opt. Express* **16**(15), 11438–11452 (2008).
23. B. J. Vakoc, R. M. Lanning, J. A. Tyrrell, T. P. Padera, L. A. Bartlett, T. Stylianopoulos, L. L. Munn, G. J. Tearney, D. Fukumura, R. K. Jain, and B. E. Bouma, "Three-dimensional microscopy of the tumor microenvironment in vivo using optical frequency domain imaging," *Nat. Med.* **15**(10), 1219–1223 (2009).
24. B. R. White, M. C. Pierce, N. Nassif, B. Cense, B. H. Park, G. J. Tearney, B. E. Bouma, T. C. Chen, and J. de Boer, "In vivo dynamic human retinal blood flow imaging using ultra-high-speed spectral domain optical coherence tomography," *Opt. Express* **11**(25), 3490–3497 (2003).
25. J. Fingler, R. J. Zawadzki, J. S. Werner, D. Schwartz, and S. E. Fraser, "Volumetric microvascular imaging of human retina using optical coherence tomography with a novel motion contrast technique," *Opt. Express* **17**(24), 22190–22200 (2009).
26. L. An, H. M. Subhush, D. J. Wilson, and R. K. Wang, "High-resolution wide-field imaging of retinal and choroidal blood perfusion with optical microangiography," *J. Biomed. Opt.* **15**(2), 026011 (2010).
27. L. Yu and Z. Chen, "Doppler variance imaging for three-dimensional retina and choroid angiography," *J. Biomed. Opt.* **15**(1), 016029 (2010).
28. M. Szkulmowski, A. Szkulmowska, T. Bajraszewski, A. Kowalczyk, and M. Wojtkowski, "Flow velocity estimation using joint spectral and time domain optical coherence tomography," *Opt. Express* **16**(9), 6008–6025 (2008).
29. R. K. Wang, L. An, S. Saunders, and D. J. Wilson, "Optical microangiography provides depth-resolved images of directional ocular blood perfusion in posterior eye segment," *J. Biomed. Opt.* **15**(2), 020502 (2010).
30. S. Makita, F. Jaillon, M. Yamanari, M. Miura, and Y. Yasuno, "Comprehensive in vivo micro-vascular imaging of the human eye by dual-beam-scan Doppler optical coherence angiography," *Opt. Express* **19**(2), 1271–1283 (2011).
31. S. Makita, Y. Hong, M. Yamanari, T. Yatagai, and Y. Yasuno, "Optical coherence angiography," *Opt. Express* **14**(17), 7821–7840 (2006).
32. S. Zotter, M. Pircher, T. Torzicky, M. Bonesi, E. Götzinger, R. A. Leitgeb, and C. K. Hitzenberger, "Visualization of microvasculature by dual-beam phase-resolved Doppler optical coherence tomography," *Opt. Express* **19**(2), 1217–1227 (2011).
33. Y. K. Tao, K. M. Kennedy, and J. A. Izatt, "Velocity-resolved 3D retinal microvessel imaging using single-pass flow imaging spectral domain optical coherence tomography," *Opt. Express* **17**(5), 4177–4188 (2009).
34. B. Potsaid, B. Baumann, D. Huang, S. Barry, A. E. Cable, J. S. Schuman, J. S. Duker, and J. G. Fujimoto, "Ultra-high speed 1050nm swept source/Fourier domain OCT retinal and anterior segment imaging at 100,000 to 400,000 axial scans per second," *Opt. Express* **18**(19), 20029–20048 (2010).

35. C. M. Eigenwillig, T. Klein, W. Wieser, B. R. Biedermann, and R. Huber, "Wavelength swept amplified spontaneous emission source for high speed retinal optical coherence tomography at 1060 nm," *J. Biophotonics* **4**(7-8), 522-528 (2011).
36. M. Gora, K. Karnowski, M. Szkulmowski, B. J. Kaluzny, R. Huber, A. Kowalczyk, and M. Wojtkowski, "Ultra high-speed swept source OCT imaging of the anterior segment of human eye at 200 kHz with adjustable imaging range," *Opt. Express* **17**(17), 14880-14894 (2009).
37. V. J. Srinivasan, D. C. Adler, Y. Chen, I. Gorczynska, R. Huber, J. S. Duker, J. S. Schuman, and J. G. Fujimoto, "Ultrahigh-speed optical coherence tomography for three-dimensional and en face imaging of the retina and optic nerve head," *Invest. Ophthalmol. Vis. Sci.* **49**(11), 5103-5110 (2008).
38. B. Potsaid, I. Gorczynska, V. J. Srinivasan, Y. L. Chen, J. Jiang, A. Cable, and J. G. Fujimoto, "Ultrahigh speed spectral / Fourier domain OCT ophthalmic imaging at 70,000 to 312,500 axial scans per second," *Opt. Express* **16**(19), 15149-15169 (2008).
39. D. Y. Kim, J. Fingler, J. S. Werner, D. M. Schwartz, S. E. Fraser, and R. J. Zawadzki, "In vivo volumetric imaging of human retinal circulation with phase-variance optical coherence tomography," *Biomed. Opt. Express* **2**(6), 1504-1513 (2011).
40. R. K. Wang, L. An, P. Francis, and D. J. Wilson, "Depth-resolved imaging of capillary networks in retina and choroid using ultrahigh sensitive optical microangiography," *Opt. Lett.* **35**(9), 1467-1469 (2010).
41. W. Wieser, B. R. Biedermann, T. Klein, C. M. Eigenwillig, and R. Huber, "Multi-megahertz OCT: High quality 3D imaging at 20 million A-scans and 4.5 GVoxels per second," *Opt. Express* **18**(14), 14685-14704 (2010).
42. T. Klein, W. Wieser, C. M. Eigenwillig, B. R. Biedermann, and R. Huber, "Megahertz OCT for ultrawide-field retinal imaging with a 1050 nm Fourier domain mode-locked laser," *Opt. Express* **19**(4), 3044-3062 (2011).
43. L. An, G. Guan, and R. K. Wang, "High-speed 1310 nm-band spectral domain optical coherence tomography at 184,000 lines per second," *J. Biomed. Opt.* **16**(6), 060506 (2011).
44. H. C. Hendargo, M. Zhao, N. Shepherd, and J. A. Izatt, "Synthetic wavelength based phase unwrapping in spectral domain optical coherence tomography," *Opt. Express* **17**(7), 5039-5051 (2009).
45. S. L. Jiao, R. Knighton, X. R. Huang, G. Gregori, and C. A. Puliafito, "Simultaneous acquisition of sectional and fundus ophthalmic images with spectral-domain optical coherence tomography," *Opt. Express* **13**(2), 444-452 (2005).

1. Introduction

Optical coherence tomography (OCT) [1] is known to have the capability of providing depth resolved information of biological tissue with a spatial resolution at micrometer scale [2,3]. Driven perhaps by tremendous commercial and research potentials, numerous efforts have been paid to develop retinal OCT, including technical developments and clinical applications. In the technical aspect, the increase of the system imaging speed has been always a momentum because the higher imaging speed could bring the advantage of minimizing the motion artifacts in human imaging studies, facilitating the clinical interpretation of OCT data/images. Since the initial report of OCT in 1991 [1], its development can be roughly classified into three generations in terms of the imaging speed. The first generation (1g) is the time domain OCT (TDOCT) [4] that is capable of only up to ~8,000 A-lines per second (with the most of systems having up to 2 kHz A-scan rate), which is mainly restricted by the employment of a mechanically scanning mirror in the reference arm to provide depth-resolved axial information of the sample. With this imaging speed, it is sometimes difficult for TDOCT to achieve 3D scanning for *in vivo* imaging applications. For example, in retinal imaging, only several cross sectional images could be captured before the eye blinking and movements happen [5] which is inevitable for human studies. To increase the imaging speed, a new interferogram detection scheme, Fourier domain OCT (FDOCT), is proposed to directly achieve depth resolved reconstruction of the biological tissue without the need of mechanically scanning the reference arm [6,7], which development represents the 2nd OCT generation (2gOCT). In FDOCT, the interference spectrograms are detected either with a broad band light source and a high speed spectrometer (i.e., spectral domain OCT [SDOCT]) [6,7] or a wavelength swept laser and ultrahigh speed photo-detector (swept source OCT [SSOCT]) [8,9]. Compared to TDOCT, FDOCT has proven to have dramatically improved system sensitivity [10-12], thereby affording much higher imaging speed while without losing useful information about the sample. Beginning in 2002 [13], FDOCT has gradually become dominant in retinal OCT development [14-20], allowing a scanning rate at dozens of kilo-A-lines per second (up to ~40 kHz). With this imaging speed, it is possible to visualize the sample in a 3D mode, offering much flexibility in the comprehensive analysis and quantification of the sampled volume. In addition, based on the high speed FDOCT, several

novel imaging processing algorithms have been made possible to achieve *in vivo* 3D functional imaging of the tissue sample, for example the blood flow and microvasculature imaging [21–33].

Although 2gOCT has been demonstrated great success in the past few years, the imaging speed is still a barrier to achieve satisfactory 3D imaging on untrained patients due to the inevitable motion during the *in vivo* imaging. It is now clear that one of the solutions to reduce the motion artifacts in the final results is to further improve the system imaging speed. Recently, the ultrahigh speed (hundreds of kHz line rate) FDOCT system (the third generation (3g) OCT) becomes more and more attractive by employing the frequency domain mode locking (FDML) technology [34–37] in SSOCT and high speed line scan CMOS camera in SDOCT [38–40]. Though the FDOCT systems running at several MHz scanning speed have been reported in the research laboratories, none of them has demonstrated adequate imaging performance for retinal imaging applications. For example, the 20 MHz system demonstrated in [41] was based on a 1310 nm swept laser source, which may not be utilized in human retinal imaging due to its relatively high water absorption compared to its lower wavelength counterparts. The 1.3 MHz 1050 nm system reported in [42] suffers from the poor axial resolution ($\sim 25\ \mu\text{m}$). So far, the fastest retinal FDOCT system, which can maintain both the high axial resolution ($\sim 7\ \mu\text{m}$) and the ultrafast imaging speed, is reported in [34], in which the authors developed an 1- μm SSOCT system running at ~ 400 kilo-A-lines per second, realized by combining FDML with a multi-spots detection strategy. This reported system is possible to further improve its imaging speed to 684 kHz [42]. In doing so, however, it needs to sacrifice the wavelength sweeping range, thus reducing the axial resolution to $\sim 16\ \mu\text{m}$ [42]. Notwithstanding, SSOCT in the 1- μm wavelength band is reported to be capable of providing promising results for retinal imaging [34,42], however, the commercial utilization of such SSOCT is still yet to be approved by the FDA. Currently, the commercially available retinal OCT systems are still based on SDOCT, with the imaging speed directly determined by the camera employed in the spectrometer. Until now, the fastest retinal SDOCT system reported is a system working at 312 kHz A-line rate [38]. However, to reach 312 kHz, it has to sacrifice the spectral resolution by using a part of the CMOS sensor array (576 pixels out of 4096 pixels). In consequence, the detectable depth is shallow (~ 2 mm in air) and the system sensitivity rolling off is relatively high (~ 25 dB over 2-mm ranging distance). To further increase the imaging speed while maintaining the system axial resolution at less than $10\ \mu\text{m}$, the acceptable performances, e.g., system sensitivity rolling off and detectable depth range, are still a big challenge for the development of retinal SDOCT system.

In this paper, we describe a newly developed ultrahigh speed 850 nm SDOCT for ophthalmology applications. Based on a previously reported SDOCT imaging speed boosting technology [43], the imaging speed of our SDOCT system was significantly improved by employing two high speed CMOS cameras in the system, enabling an imaging speed of 500,000 A-lines per second. Compared to the prior ultrahigh speed system, such as [38], the improvement of the imaging speed in the proposed SDOCT system is a result of fully utilizing the dead time of the CMOS cameras rather than sacrificing the camera integration time. With such ultrahigh imaging speed, we propose two scanning protocols to perform dense sampling for the 3D data set: 1) fast B-frame imaging mode, and 2) large field of view imaging mode. The former is able to minimize the motion artifacts during the *in vivo* imaging while the latter enables better evaluation of the overall retinal status. To better interpret the large field of view images in a depth-resolved en-face fashion, we propose a method to flatten the 3D data set according to the inner segments of photoreceptor (ISP) that is a relatively high reflecting layer. To the best of our knowledge, this is the fastest retinal SDOCT system reported so far with a high axial resolution of less than $10\ \mu\text{m}$ in air.

2. System configuration

The schematic of our ultrahigh speed SDOCT system was illustrated in Fig. 1, in which a superluminescent diode was utilized as the light source, which provided a spectral bandwidth of 45 nm centered on 842 nm, resulting in a theoretical $\sim 7\ \mu\text{m}$ axial resolution in air. The

output light was coupled into a fiber-based Mach-Zehnder interferometer through a 20/80 fiber coupler, with 20% going to the sample arm and 80% to the reference arm via optical circulators. In the sample arm, the combination of collimator, scan-lens and ocular objective lens provided $\sim 16 \mu\text{m}$ lateral resolution on the surface of retina. In the reference arm, a 20 mm water cell was utilized to approximately match the aqueous humor in the human eye, facilitating the dispersion compensation during the post-data processing. The lights backscattered from the sample and reflected from the reference mirror were recombined and then split into two equal portions via a 50/50 fiber splitter. The two equal portions of light were then delivered to two home-built high speed spectrometers separately. Each spectrometer was made of the same optical components: a collimator ($f = 50 \text{ mm}$), a transmission grating (1200 lines/mm), an achromatic focusing lens ($f = 100 \text{ mm}$) and a high speed line scan CMOS camera (Basler, Sprint spL4096-140k). After careful adjustment, the spectrometers delivered almost the same performance for OCT imaging (also see next section for detail).

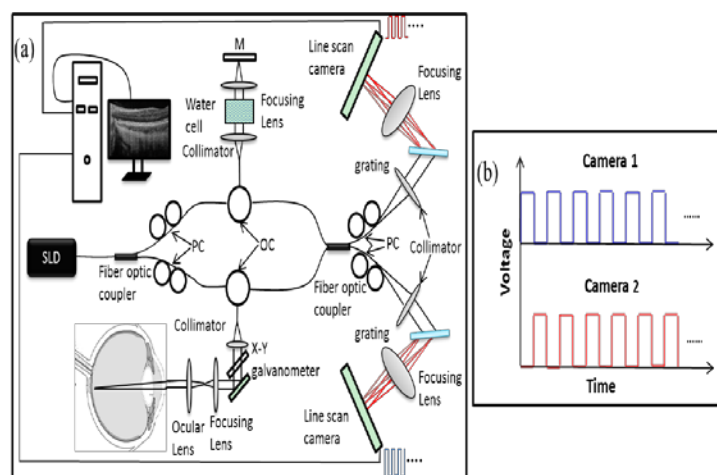


Fig. 1. (a) Schematic of the ultrahigh speed SDOCT system; and (b) the trigger signal sequences for dual-camera system. SLD: superluminescent diode; PC: polarization controller; OC: optical circulator.

The critical components of our ultrahigh speed SDOCT system are two high speed line scan CMOS cameras. The CMOS camera is able to achieve varied line scan rate through an appropriate selection of the number of pixels used for data collection, for example it is 70 kHz if the full 4096 pixels are used, while it can run at 312 kHz if only 576 pixels are selected [38]. Considering the balance between the imaging speed, axial resolution and the system detectable depth range, for each spectrometer, we selected 800 pixels out of 4096 pixels to achieve A-line capture rate of 250 kHz. Thus, when the light with a spectral bandwidth of 45 nm is detected by the 800 pixels sensor array, the specified imaging depth of the system reached $\sim 2.5 \text{ mm}$, suitable for imaging the human retina. To achieve a scanning rate of 500,000 A-lines per second, we adopted the imaging-speed boosting methodology proposed in [43], in which the two cameras were precisely and sequentially controlled. Briefly, two trigger sequences were generated to precisely control the reading and recording phases of the cameras. At first, a 250 kHz square wave form (with 50% duty cycle) was generated as the trigger sequence for the first camera (illustrated in the top of Fig. 1 (b)). Within one signal cycle, the data recording was triggered when the signal is on in the first half time and the data reading otherwise. Secondly, a reversed trigger sequence to the first camera was generated as the trigger signal for the second camera (illustrated in the bottom of Fig. 1 (b)). Combining these two trigger sequences, the two cameras worked in tandem to achieve zero dead time dual-camera system as if the system realized 100% duty cycle for image recording.

Compared to the previously reported fastest retinal SDOCT system in [38], our system demonstrated two major advantages. First, the imaging speed of our system is much faster

than that of in [38] (500 vs. 312 kHz). Second, for each camera, more pixels were activated for image recording (800 vs. 576 pixels), which will facilitate deeper imaging depth (2.5 vs. 2.0 mm) for a similar axial resolution. Moreover, the light energy efficiency of the light source of our system was higher than the traditional configuration used in [38], which was achieved by two strategies. The first one was that we used the same integration time for the line scan camera as in [38]. The improvement of the imaging speed of our system was resulted from fully utilizing the camera dead time rather than sacrificing the integration time. The second one was that we employed two optical circulators in the system design to realize a Mach-Zehnder type low-coherence interferometer. This system design made almost 100% usage of the light backscattered from the sample, preventing the useful light from wasting like in a Michelson type of interferometer. However, the final sensitivity is slightly lower than that in [38], caused by the 50/50 fiber coupler used in the system (50% vs. 90% of sample light back to single camera). With these considerations, our system was able to provide a better performance in both the imaging speed and imaging depth, which will be presented further in the later section. Note that if a similar system performance to that reported in [38] is considered for the system design, it is no doubt that the proposed system would be able to achieve an imaging speed of 624,000 A-lines per second. Notwithstanding, to achieve the higher imaging speed, the price that has to be paid for the proposed system is the increased cost of the likely system, which may become a major factor in limiting its clinical applications.

3. System performance

As mentioned in the previous section, we have setup the two high speed spectrometers carefully so that they delivered almost the same system performance. Even so, it was still difficult for the two spectrometers to achieve exactly the same performance solely based on the system alignment due to the non-identical parameters of the optical components and the difficulty in controlling the polarization status in their optical paths. However, to achieve the best performance of the proposed dual-camera system, the performance of the two individual spectrometers should be identical to each other. To meet this requirement, below we adopted a spectral shaping methodology as suggested in [44] to shape the spectrograms captured by two individual spectrometers so that they gave the identical imaging performance.

It is known that the shape of the spectrum captured by the spectrometer would have strong effect on the system performance in term of side lobes when evaluating the axial resolution of the system. To better illustrate this effect, we would like to begin the discussion from the following basic OCT theory (presented by Eq. (1)), where the self-correlation and DC terms are ignored:

$$I(K) = 2S(K)E_R \int_{-\infty}^{\infty} a(z) \cos(2Knz) dz \quad (1)$$

where K is the wavenumber; n is the refractive index of the sample; $S(K)$ is the spectral density of the light source; z is the depth where the light back scattered from; $a(z)$ is the amplitude of the light; and E_R is the light reflected from the reference mirror. To extract the depth resolved information from Eq. (1), fast Fourier transform (FFT) is usually applied onto the variable K . According to Eq. (1), the captured spectrum shape of the light source will affect the performance on our dual-camera system in several aspects. At first, the light source used in our system was of non-Gaussian shaped spectrum (presented in Fig. 2 (a)) that would generate side-lobes, thus impairing the imaging quality. In addition to this, because the optical components used in the setup were not absolutely equal and the difficulty in precisely controlling the polarization status in the light paths, the light spectrum captured by the individual cameras would be slightly different (see Fig. 2 (a)), which would also result in degradation of the final system performances. To minimize these effects on the system performances, a digital spectrum shaping method [44] was utilized, in which a Gaussian function was used to digitally re-shape the measured light spectrum. After the digital spectral re-shaping, the results are presented in Fig. 2 (b), which gives the axial point spread functions

(PSF) obtained by placing the reference mirror at 0.5 mm away from the zero delay line. The red and blue curves are corresponding to the PSF of each of two spectrometers (normalized to the first camera, the red curve) before applying the spectrum re-shaping, while yellow and green curves are results after the spectrum re-shaping (normalized to the first camera, the yellow curve). As we can see, the spectrum shaping brought two benefits to the performance of our system. At first, the sidelobes (targeted by the red arrows in Fig. 2 (b)) were sufficiently minimized. Compared to the red and blue curves, the yellow and green curves are much smoother. Secondly, the differences of the PSFs between two spectrometers were greatly reduced. Zooming into the region marked by the black square (see the insert in Fig. 2 (b)), the difference between the green and yellow curves are much smaller compared to the difference between the red and blue curves. These results demonstrate that after spectral reshaping, the PSFs of two cameras are almost exactly the same except the noise region. However, the spectral shaping would cause ~1dB sensitivity loss as compared to that in [38].

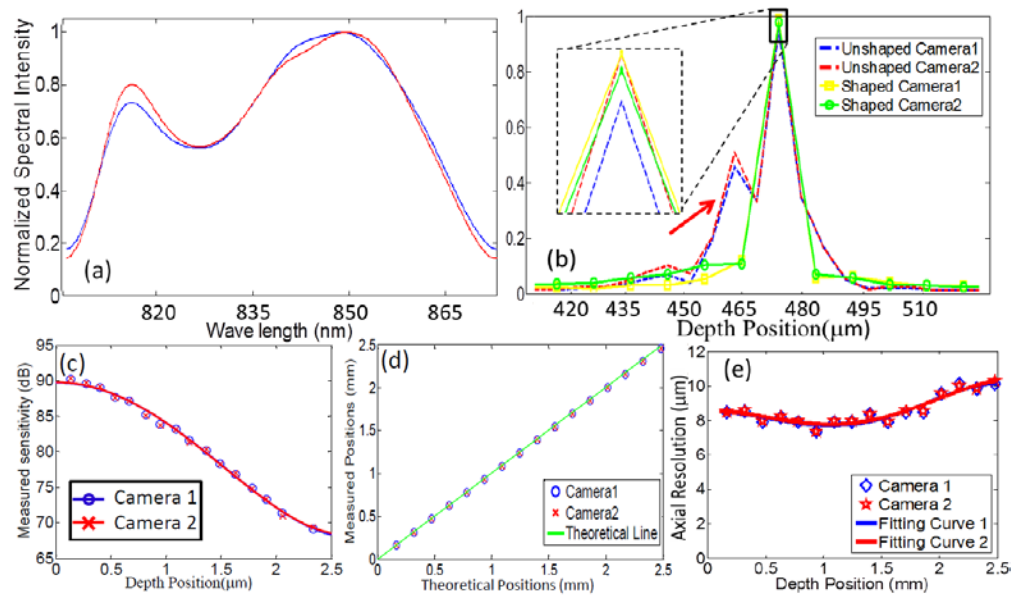


Fig. 2. System performance of the ultrahigh speed SDOCT. (a), light source spectrums captured by the two spectrometers of the system; (b) the PSF of the two spectrometers before (red and blue) and after (yellow and green) the digital beam shaping. (c) the system sensitivity falling off curves. (d) the measured optical delay line positions. (e) the measured system axial resolution.

To further evaluate the performance of the proposed ultrahigh speed SDOCT system, a sensitivity testing experiment was performed. In doing so, a reflecting mirror was placed in the sample arm to simulate the sample. The light power in the sample arm was measured at 0.8mW, consistent with the retinal experiments discussed later. A 40 dB OD filter was also installed into the sample arm to reduce the light reflected from the mirror. To measure the sensitivities at different time delays, the reference mirror was moved step by step from ~0.15 mm position to the ~2.4 mm position (~0.15 mm interval). At each position, the interferogram was recorded and converted from the wavenumber space to the time space (i.e., depth ranging space). Thus, the measured signal to noise ratio (SNR) at each position plus 40 dB (reduced by the OD filter) would be the sensitivities of the system. The peak positions were also recorded as the measured optical delay line. For each peak, full width at half max (FWHM) was calculated as the axial resolution in air. The results are presented in Figs. 2 (c), (d) and (e), respectively. As we can see, the two individual spectrometers have almost the same performance under the control of the trigger sequences as discussed in the previous section. Both of them achieved ~90 dB around the zero-delay line and ~83 dB at 1.2 mm the imaging

depth position (Fig. 2 (c)). The measured and the fitted system-sensitivity falling-off curves are almost exactly the same. As to the measured peak position, both spectrometers provided the same results, as illustrated in Fig. 2 (d). Figure 2 (e) demonstrated the measured axial resolution, where it can be seen that both spectrometers delivered an averaged $\sim 8.5 \mu\text{m}$ axial resolution up to 1.8 mm imaging depth and $\sim 10 \mu\text{m}$ at deeper imaging depth in the air.

4. In vivo retinal imaging results

To demonstrate the capability of the proposed ultrahigh speed SDOCT system, a series of in vivo experiments were performed on a healthy volunteer in our laboratory. Two imaging protocols, i.e., high speed scanning mode and large field of view scanning mode, were designed to achieve visualizations of human retina to meet the requirements of different clinical goals. For the first scanning protocol, each camera was set to capture 250 A-lines along the fast axis, resulting in 500 A-lines within each B-frame image. Under this circumstance, the camera was theoretically able to achieve $\sim 1 \text{ kHz}$ B-frame capturing rate. However, considering the data transmission and scanning mirror flying back time, the practical maximal B-frame scanning rate that the system can achieve was 700 Hz. With this imaging rate, we captured 500 B-frames along the slow axis to make up of one isotropic 3D scan, covering an area of $4 \times 4 \text{ mm}^2$ on the retina. The total imaging time for such 3D scan was only cost $\sim 0.72\text{s}$, which is short enough to prevent possible motion artifacts caused by the movements of the eye and head.

The second scanning protocol was designed to achieve a large field of view ($\sim 10 \times 10 \text{ mm}^2$) for retinal imaging with a homogeneous dense sampling along both the fast and slow axes. Assuming that the space interval between adjacent A-lines is half of the system lateral resolution ($\sim 16 \mu\text{m}$), 1200 A-lines are required along both the fast and slow axes to finish one typical 3D scan. Under this condition and with 80% duty cycle used for the fast-scanner, the proposed SDOCT system was capable of running at $\sim 320 \text{ Hz}$ B-frame imaging rate, leading to about 4 seconds in total to perform one 3D scan. In all the experiments performed in this study, the power of the light incident on the cornea was $\sim 0.8 \text{ mW}$, which is consistent with the safe ocular exposure limits set by the American National Standards Institute (ANSI) [45].

4.1. Scan protocol 1: High speed isotropic dense sampling 3D retina imaging

The imaging speed is critical for *in vivo* ophthalmology applications. Both the patient examining experience and the final imaging results will benefit from the higher imaging speed. Currently, the imaging speed for commercially available retinal OCT systems is up to 40 kHz A-scan rate, taking about 3-4 seconds to finish one 3D scan. However, the captured 3D data set normally gives less accurate definition on the scanned tissue volume because the sampling density is normally scarce compared to the system resolution, leading to some difficulties in interpreting the imaging results even after sophisticated algorithms are applied to enhance the image readability. The total examining time of $\sim 3\text{-}4$ seconds for one 3D imaging is almost to a limit for most of the untrained patients. Even within this time period, the subject movements are inevitable and pose a significant challenge for acquiring satisfactory data set for clinical data interpretation. With the proposed high speed isotropic dense sampling scanning protocol, the current SDOCT system is able to bring at least two main advantages to the *in vivo* retinal imaging: 1) sampling is homogeneous and dense on retina (500 A-lines covering 4 mm on both the fast and slow axes), which makes it possible to extract arbitrarily oriented cross sectional images [42]; 2) the examination time is short ($\sim 0.72 \text{ sec}$), which helps to minimize the inevitable movements of the eye and head. The imaging results by using the first scanning protocol were demonstrated below.

Before giving the imaging results using the first scanning protocol, we present a comparison of results obtained using single camera-based and dual-camera based spectrometers, respectively. Shown in Fig. 3 are the results obtained from (a) the combined use of the two cameras as proposed here, and (b) from the data captured by the camera 1 (image from the camera 2 is not shown here as it is essentially identical to that from camera

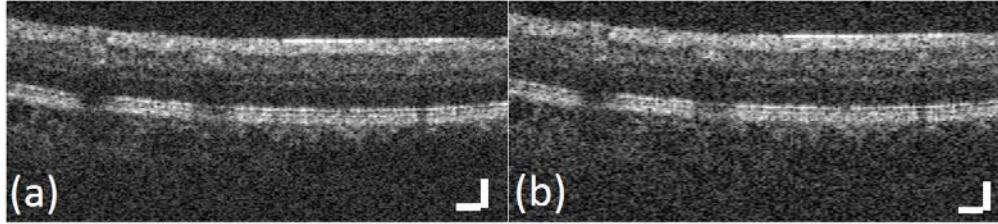


Fig. 3. B-frame retinal images obtained from (a) the combined use of two spectrometers, and (b) the spectrometer that employed the camera 1, respectively. (Scale bar = 200 μm)

1). It is obvious that Fig. 3(a) shows better image quality than that in Fig. 3(b). The improved image contrast and definition were the direct result of higher A-line density that was made possible by the dual-camera system (500 vs. 250 A-scans).

Figure 4(a) demonstrates the typical cross sectional images (i.e., the B-frame images in the fast axis) captured at the location marked by the red line in Fig. 4(d). Because of the dense sampling along the slow-axis, the averaging process is possible between adjacent B-frames in order to increase the signal to noise ratio (SNR), thus the definition of the images. In Fig. 4(a), the images (i), (ii), (iii), (iv) and (v) corresponds to the averaging results between one, three, six, nine and twelve B-frames, respectively. As we can see, with the increase of numbers participated in the averaging, the noise was significantly reduced from (i) to (v). Figure 4(b) shows the cross sectional frames along the slow axis, representing the location marked by the green line in Fig. 4 (d). The imaging quality of the slow-axis cross-sectional images is comparable with that of the fast-axis ones. This benefit is directly resulted from the dense sampling along the slow axis and the fast imaging speed that the system can afford. In Fig. 4(b), only one small movement was noticed (pointed by the white arrow), indicating that our data set was almost free from the movements, making the averaging process between slow-axis cross-sectional images possible so that the image quality is enhanced for better data interpretation.

The imaging results of Figs. 4(a) and 4(b) indicate that the image quality can be enhanced by averaging the adjacent cross-section images in either the fast or slow axes. However, with the increase of numbers of images participated in the averaging, the results become blurrier, thus the image resolution is sacrificed. This becomes more severe when a large number of frames are participated, e.g. $n = 12$ (Fig. 4a(v) and Fig. 4b(v)). To balance, we propose to average frames along both the directions, i.e. fast and slow axes, so that the image quality is enhanced while the degradation of imaging resolution is minimized. Figure 4(c) shows the images resulted from averaging two, three and four frames on both the fast and slow axes. As we can see, the image SNR was significantly improved while the resolution distortion is much smaller when compared to those averaged from a single axis alone. Except the SNR improvement, another benefit brought by the spatial averaging is the reduction of speckle noises. Please refer to [42] for details.

Finally, we used the results processed by averaging adjacent three frames on both the fast and slow axes, e.g., Fig. 4c(iii), to produce the OCT fundus images [45], which result is shown in Fig. 4(d). Due to the short examination time required for one 3D scan (~ 0.72 sec), there are no noticeable discontinuities of retina in Fig. 4(d) caused by the subject movement (also see [Media 1](#), which was played back in an en-face fashion at 10 fps). Because of the dense sampling on both directions, even the small retina features could be captured. For example, the small retinal vessel branches (pointed by red arrows) could be clearly visualized in Fig. 4(d). Figure 4 (e) demonstrates the 3D rendered volumetric structure image of scanned human retina. Except one small distortion (pointed by the blue arrows) caused by a slight movement, the most other regions of the rendered 3D are quite smooth, demonstrating the value of the fast imaging speed.

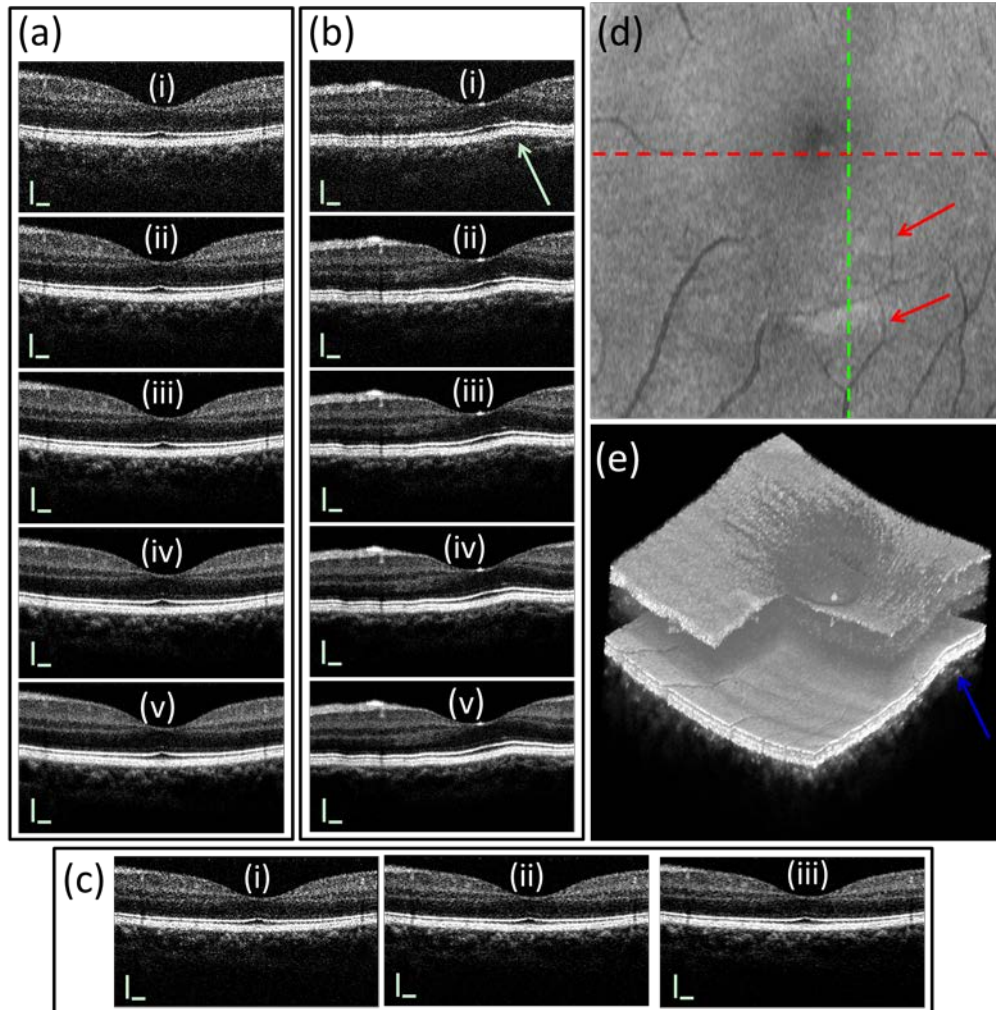


Fig. 4. *In vivo* experimental results obtained by high speed isotropic dense sampling 3D retinal imaging. (a) Cross-sectional images along the fast scan-axis, where (i) to (v) correspond to the results after averaging adjacent one, three, six, nine and twelve fast-scan images, respectively. (b) Cross-sectional images along the slow axis, where (i) to (v) are resulted from averaging adjacent one, three, six, nine and twelve slow cross-sectional images, respectively. (c) Cross sectional images, where (i) to (iii) are resulted from averaging adjacent two, three and four frames along both the fast and slow axes. (d) OCT fundus image [also see Media 1]. (e) 3D rendering volumetric image. (Scale bar = 200 μm)

4.2. Scan protocol 2: wide field of view isotropic dense sampling 3D retina imaging

In ophthalmology clinical applications, it is sometimes essential for a FDOCT system to achieve the visualization for a large field of view because it may provide overall assessment about the retina status and decrease the possibility of missing the abnormal points presented by eye diseases. Restricted by short acceptable examining time (typically 3-4 seconds) for *in vivo* diagnosis, how many A-lines are allowed in both the fast and slow axes for imaging the sample with a large field of view directly depends on the system imaging speed. The faster imaging speed the FDOCT system can achieve, the larger the field of view it can realize [42] under the condition that the same density of A-line sampling is permitted. Considering that the lateral resolution of our SDOCT system is $\sim 16 \mu\text{m}$ and at least two points were required to

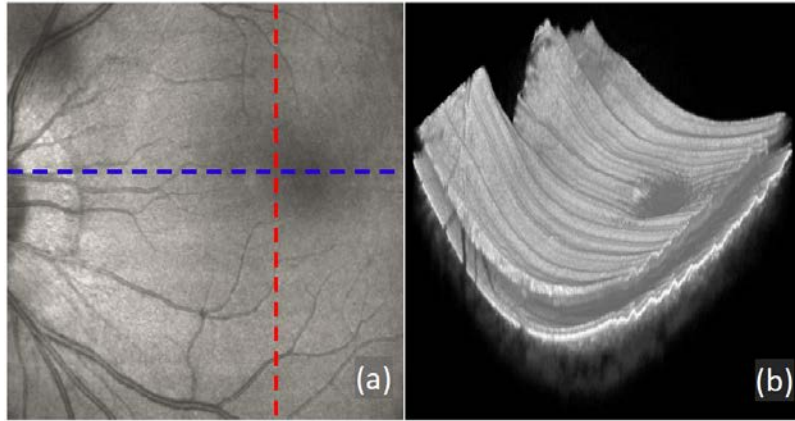


Fig. 5. *In vivo* results of a large field of view isotropic dense sampling retina imaging. (a) OCT fundus image. (b) 3D rendering volumetric image.

cover the beam spot, we used 1200 A-lines along both the fast and slow axes to capture a region covering an area of $\sim 10 \times 10 \text{ mm}^2$ on the retina. The results are presented in Figs. (5), (6) and (7).

Figure 5 (a) is the OCT fundus image, obtained through integrating the OCT signals along the depth direction. Due to the large imaging field of view, it is possible to visualize both the fovea region and part of the optical nerve head at one single scan. Figure 5(b) shows the 3D

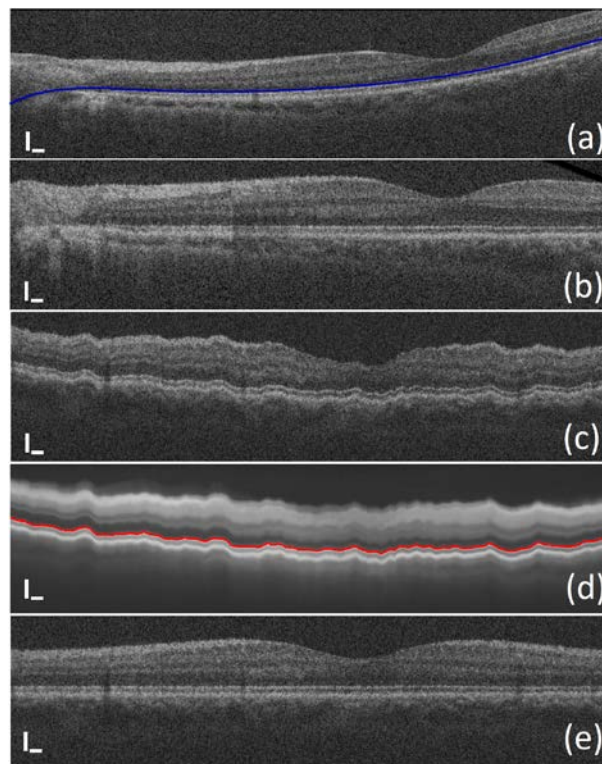


Fig. 6. (a) One typical fast B-scan cross sectional image. (b) Processed B-scan image after flattening according to the ISP layer. (c) One typical slow axis cross sectional image. (d) Collapse-averaged slow-axis image. (e) Finally processed slow-scan image. Scale bar = $200\mu\text{m}$

volumetric rendering of the large area data set. Though it can provide more depth resolved information about the retina structure, the fundus curvature of the eye ball and the inevitable movements during the examination time period of ~4 sec prevent it from being evaluated, particularly when the depth-resolved en-face view of the scanned tissue volume is required.

To compensate for the retinal surface curvature and the subject movement, we propose to flatten the original images in order to better present the depth-resolved en-face views of a large field of view. First of all, for each cross sectional image captured along the fast scanning axis [e.g., Fig. 6(a) that represents the position marked by the blue line in Fig. 5(a)], the relatively high reflecting ISP layer [the blue curve in Fig. 6(a)] was identified, which was then used as the reference to compensate the curvature of the retina surface in each fast-scan B-frames. The result is shown in Fig. 6(b), where it can be seen that the curvature was clearly eliminated. Secondly, we compensated the small drifts between fast B-frames caused by the movements of patient during the *in vivo* examination. To do this, we worked on the slow scan axis direction. For example, Fig. 5 (c) is a typical cross sectional image along the slow axis direction extracted from the position marked by the red line in Fig. 5(a). Because of the relatively long examination time (~4 sec), artifacts caused by small sample movements are evident, resulting in a fluctuation pattern. To correct these eye motions, all the flattened cross sectional images obtained in the first step (described above) were averaged along the fast scan direction to produce one averaged slow-scan cross section image, i.e., the 3D data set was collapse-averaged along the fast axis. This result is shown in Fig. 6(d). Because the flattening process in the first step used the ISP layer as the reference, the collapse-averaging enhanced dramatically the edge of the ISP layer (marked by the red curve). Finally, we used this ISP edge curve as the second reference to re-align all the fast-B-frames. Figure 6(e) is an example of flattened slow-axis cross section from Fig. 6(c), where it can be seen that all motion drifts were successfully removed, resulting in a high performance cross sectional image which is similar to the fast-scan B-frame image (Fig. 6(b)). After these flattening procedures, the processed 3D data set is now ready for further detailed visualization.

Figure 7(a) is the 3D volumetric rendering of the large scanned area after the data set was flattened according to the ISP layer along both the fast and slow axes. Compared to Fig. 5(b), Fig. 7(a) revealed more intuitive view of morphology for the human eye. For example, the thickness of the retinal para-fovea region (pointed by the white arrow) is thicker than that of the peri-fovea region (pointed by the black arrow). Another benefit brought by the flattened OCT data set is the ability to visualize the depth-resolved fundus images according to different depth locations (see [Media 2](#), which is played back at 10 fps in an en-face fashion). From this movie, the still images are presented in Figs. 7(b)-(f), corresponding to the depth positions at 440 μm above, 295 μm above, 15 μm above, 50 μm below and 130 μm below the ISP layer, respectively. These images reveal detailed, but different morphological patterns located at different retinal or choroidal depth positions. Figure 7(b) is the superficial layer cutting through the nerve fiber layer around the para-fovea region, in which the nerve fiber bundles can be easily appreciated. In Fig. 7(c), a number of blood vessels can be identified. In Fig. 7(c), the blood-vessel-like pattern is appeared, which are artifacts resulted from the shadow below the retina blood vessels due to the light absorption by the blood within them. This shadow artifact is directly responsible for the contrast in the integrated OCT fundus image (demonstrated in Fig. 5(a)). Figures 7(e) and (f) are the depth-resolved fundus images cutting through the layers, where the medium and big choroidal blood vessels are located. The size of the blood vessels seen in Fig. 7(f) (pointed by the red arrows) is much bigger than those seen in Fig. 7(e) (pointed by the blue arrows). The associates movie ([Media 2](#)) flying from the top to the bottom provides further detailed assessment of fundus images at different depth locations, which can be particularly useful in the clinical diagnosis. However, there is a practical concern associated with the use of the proposed flattening method to correct the motion artifacts in patient imaging (e.g. drusen patients). In this case, because of the irregular shape of the ISP layer, further study is needed to assess the feasibility of the flattening approach.

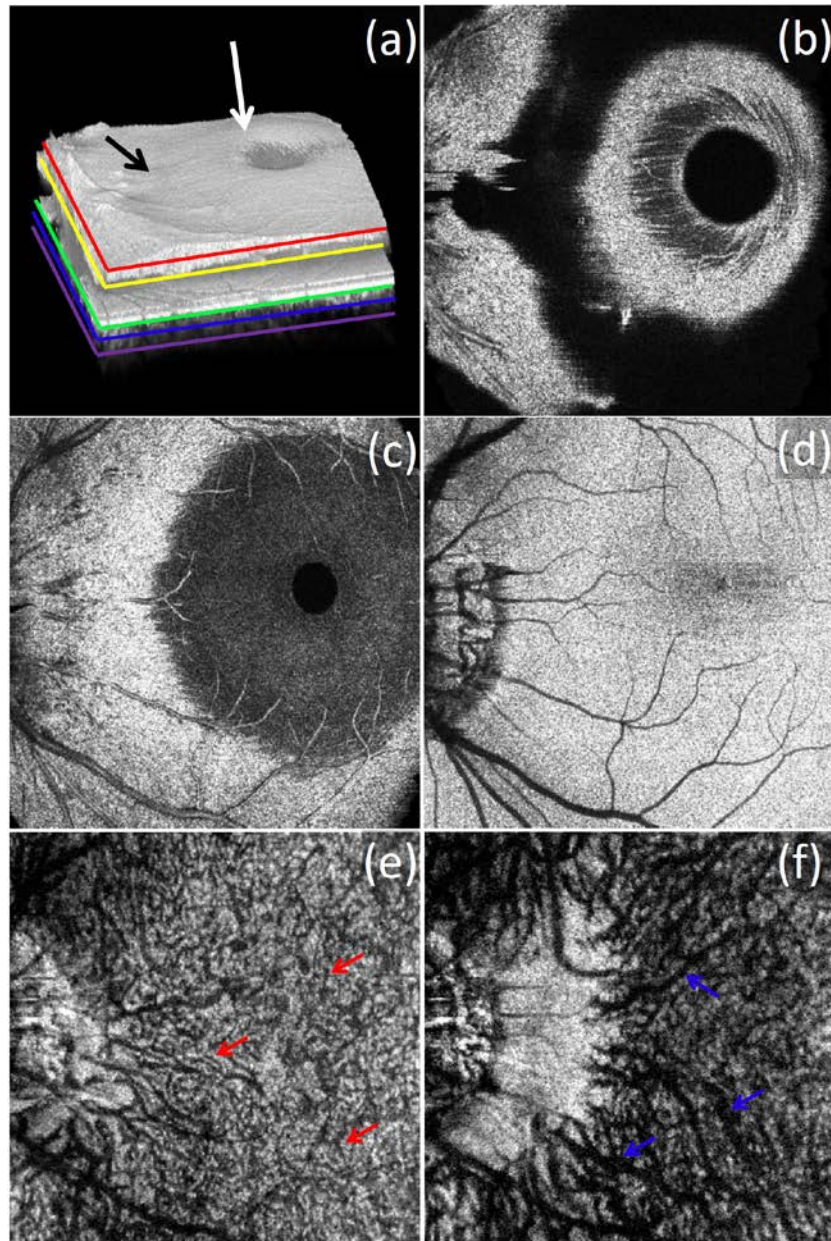


Fig. 7. After flattening the data set according to the ISP layer on both the directions, ultrahigh speed SDOCT provides ability for comprehensive assessment of the retina status over a large field view. (a) 3D rendered volumetric image. (b) to (f) are typical depth resolved fundus (en-face) images, which are corresponding to the depth positions marked by the red, yellow, green, blue and purple lines in (a). [Also see [Media 2](#).]

5. Conclusion

In conclusion, we demonstrated a newly built ultrahigh speed 850 nm SDOCT system for *in vivo* human retinal imaging applications. Through sequentially controlling two high speed CMOS line scan cameras, the new system is able to achieve half megahertz A-line scan rate, which is at least ten times faster than that of fastest commercially available FDOCT systems. A number of *in vivo* imaging experiments has been conducted to demonstrate the superior

imaging performance delivered by the proposed system. Two scanning protocols were proposed for different imaging applications: 1) ultrafast imaging mode, and 2) wide field of view imaging mode. The former provided an imaging speed of 700 Hz B-frame rate to isotropically sample a small area ($4 \times 4 \text{ mm}^2$) of the retina with a sampling density at 500 A-lines at both the fast and slow axes. The total 3D imaging time was only 0.72 sec, short enough to minimize the motion artifacts caused by the subject movement. We also demonstrated that the dense sampling make it possible to perform the two directional averaging process that significantly enhances the image SNR and reduces the speckle noise while minimizing the degradation of the imaging resolution. However, it should be noted that the SNR enhancement could also be achieved by the increase of the camera integration time, albeit with a decreased system imaging speed. The second scanning protocol gave isotropic dense sampling over a large field of view ($\sim 10 \times 10 \text{ mm}^2$), providing ability to assess the overall status about the retina. For better visualization, the obtained 3D large field of view data was flattened according to the ISP layers in both the fast and slow axes, from which the depth resolved fundus images can be easily appreciated.

Acknowledgments

This work was supported in part by research grants from the National Heart, Lung, and Blood Institute (R01 HL093140), National Institute of Biomedical Imaging and Bioengineering (R01 EB009682), and the American Heart Association (0855733G). The content is solely the responsibility of the authors and does not necessarily represent the official views of grant giving bodies.